MNRAS **000**, 1–8 (2018) Preprint 13 September 2018 Compiled using MNRAS LATEX style file v3.0

AGN-driven quenching of satellite galaxies

Gohar Dashyan,[1]★ Ena Choi,[2,3] Rachel S. Somerville[2,4]
[1] *Sorbonne Universités, UPMC-CNRS, UMR7095, Institut d'Astrophysique de Paris, F-75014 Paris, France*
[2] *Department of Physics and Astronomy, Rutgers, The State University of New Jersey*
[3] *Department of Astronomy, Columbia University, 550 W 120th Street, New York, NY 10027, USA*
[4] *Center for Computational Astrophysics, Flatiron Institute, 162 5th Avenue, New York, NY, 10010, USA*

Accepted XXX. Received YYY; in original form ZZZ

ABSTRACT

We explore the effect of active galactic nucleus (AGN) feedback from central galaxies on their satellites by comparing two sets of cosmological zoom-in runs of 28 halos with masses that range from 10^{12} to $10^{13.4}$ $M_\odot$ at $z = 0$, with (wAGN) and without (noAGN) AGN feedback. Our noAGN model includes stellar feedback from multiple processes, including powerful winds from supernovae, stellar winds from young massive stars, and AGB stars, as well as radiative heating within Strömgren spheres, additional heating effects due to the presence of metals, including grain photoelectric heating and metallicity-dependent from the cosmic X-ray background. Our wAGN model is identical except that it also includes a model for black hole seeding and accretion, as well as AGN feedback via high-velocity broad absorption line winds and Compton/photoionization heating. We show that the inclusion of AGN feedback from the central galaxy significantly affects the star formation history and the gas content of the satellite galaxies. The difference between the two sets extends as far out as a few times the viral radius of the central galaxy.

Key words: methods: numerical – galaxies: evolution – galaxies: active

1 INTRODUCTION

The process by which star formation ceases in galaxy is called *galaxy quenching*. The quenching mechanisms, i.e. the processes that prevent gas from cooling and/or forming stars, as well as their relative importance, are still a topic of active investigation.

Theoretical models of galaxy formation implemented in semi-analytical models and cosmological hydrodynamical simulations are now able to reproduce fairly well the observed stellar mass functions and luminosity functions of galaxies (see Somerville & Davé 2015 for a review). This good agreement has been obtained by tuning free parameters and the use of subgrid recipes for baryonic physics such as star formation, stellar feedback and active galactic nucleus (AGN) feedback. Another more stringent and challenging constraint for galaxy formation and evolution models is given by the internal and environmental statistical correlations of quiescent galaxies. Peng et al. (2010) suggested that two distinct processes are operating, "mass quenching", which is independent of environment, and "environment quenching", which is independent of internal properties such as stellar mass. Peng et al. (2012) suggested that the fraction of quiescent centrals depends only on stellar mass, whereas the fraction of quiescent satellites depends on both mass and environment.

Various environmental processes, gravitational or hydrodynamical, could quench satellite galaxies. Tidal forces from the host halo can strip mass from the satellite (Dekel et al. 2003; Wetzel & White 2010), and frequent high speed encounters with neighboring galaxies can tidally heat satellites (Farouki & Shapiro 1981; Moore et al. 1998). Ram pressure from the hot gas from the host halo and the high orbital velocity of the satellite can also strip or heat the gas from the satellite (Gunn & Gott 1972; Tonnesen & Bryan 2009). Strangulation or starvation, a more gradual process, is the lack of accretion of new gas (Larson et al. 1980). In semi-analytical models, environmental processes are described with simplified recipes where galaxies stop accreting new gas from the hot halo or the intergalactic medium once they become satellites. This prescription overproduces the fraction of quiescent satellites (Kimm et al. 2009). The relative importance of these environmental processes is still unclear. So is their significance with respect to internal processes, since these satellites are also affected by feedback from stars and potential AGN, which can even enhance the environmental processes (Bahé & McCarthy 2015). Furthermore, in the hierarchical structure formation scenario, galax-

★ E-mail: dashyan@iap.fr

ies join more and more massive systems, so much so that external and internal processes are connected and hard to disentangle.

Several studies have claimed to detect a correlation between properties of galaxies, such as morphology, gas content, star formation rate, and those of neighboring galaxies. This effect, called *galactic conformity* was first observed for satellites of larger central galaxies: satellites of passive host galaxies are more likely to also be passive relative to their counterparts around star-forming hosts, at fixed group mass (Weinmann et al. 2006; Kauffmann et al. 2010; Wang & White 2012; Phillips et al. 2014; Knobel et al. 2015). This suggests that quenching mechanisms for central galaxies also impact the satellite galaxies. A detection of conformity signal on projected distances of up to 4 Mpc was presented in Kauffmann et al. (2013). However, it should be noted that subsequent studies have questioned the validity of past detections due to selection biases or possible errors in estimating halo masses (Campbell et al. 2015; Sin et al. 2017; Calderon et al. 2018; Tinker et al. 2018 ; see section 6.2.2 of Wechsler & Tinker 2018 for a recent review). The physical origin of galactic conformity is still unclear. Hearin et al. (2015, 2016) suggest that the large-scale conformity signal is a detection of central galaxy assembly bias, *i.e.* the fact that the formation histories of dark matter halo are spatially correlated. Another physical explanation, suggested by Kauffmann (2015, 2018), is that gas is heated over large scales at early times by AGN feedback.

In the context of the formation of massive elliptical galaxies, observations have established that early-type galaxies form and become red and dead early but continue to grow in mass and size without much late star formation (e.g. Daddi et al. 2005; Trujillo et al. 2006; Buitrago et al. 2008; Szomoru et al. 2012. These observations favor a two-phase formation scenario (Naab et al. 2007; Oser et al. 2010). In this scenario, the progenitors build the bulk of their mass in a short but intense starburst event at $z > 2$. Then, a progressive process of mergers with satellites and accretion of old stars produces the stellar envelopes resulting in a significant size growth (Bezanson et al. 2009; van Dokkum et al. 2010; Hirschmann et al. 2012; Sales et al. 2012). Therefore, the gas and stellar content of these satellites is an essential parameter for the size growth and the amount of gas available for late star formation in this two-phase formation scenario.

Recent hydrodynamical simulations by Choi et al. (2017, 2018) showed that the inclusion of AGN feedback effectively quenches the star formation in massive galaxies, transforming blue compact galaxies into compact quiescent galaxies. AGN feedback also removes and prevents new accretion of cold gas, shutting down in-situ star formation and causing subsequent mergers to be gas-poor. Gas poor minor mergers then build up an extended stellar envelope. AGN feedback also puffs up the central region through the fast AGN driven winds as well as the slow expulsion of gas while the black hole (BH) is quiescent. Without AGN feedback, large amounts of gas accumulate in the central region, triggering star formation and leading to overly massive blue galaxies with dense stellar cores.

In this paper, we use the two sets of cosmological zoom-in simulations run by Choi et al. (2017) to explore the effect of AGN feedback from central galaxies on their satellites or neighboring galaxies. We compare two zoom-in runs of of 28 halos with masses that range from 10^{12} to $10^{13.4}$ $M_{\odot}$, with (wAGN) and without (noAGN) AGN feedback. We show how the star formation in these satellite galaxies is efficiently quenched by the central AGN.

This paper is structured as follows. In Section 2, we describe the simulations used as well as our halo finding and tracking methods, and in Section 3, we present the results of our analysis. We discuss and summarize our results in Section 4.

2 SIMULATIONS AND METHODS

In this section, we give a brief overview of the physics relevant to our study. A more detailed description of the simulations can be found in Choi et al. (2017).

2.1 Code basics and setup

The simulations are run with a modified version of the parallel smoothed particle hydrodynamics (SPH) code GADGET-3 (Springel 2005), SPHGal (Hu et al. 2014), that includes a density-independent pressure-entropy SPH formulation (Hopkins 2013). To further improve over standard SPH, we adopt the Wendland C^4 kernel with 200 neighboring particles. We also include the improved artificial viscosity implementation presented by Cullen & Dehnen (2010) and an artificial thermal conductivity according to Read & Hayfield (2012) in order to reduce the noise in pressure estimates in the presence of strong shocks. Finally, a time-step limiter is employed according to Saitoh & Makino (2009) and Durier & Dalla Vecchia (2012) to ensure that neighboring particles have similar time steps and that ambient particles do not remain inactive when a shock is approaching.

2.2 Star formation and stellar/supernova feedback

Star formation and chemical evolution are modelled as described in Aumer et al. (2013), which allows chemical enrichment by winds driven by Type I SNe, Type II SNe, and asymptotic giant branch (AGB) stars. Eleven species of metals are tracked explicitly, and the net cooling rates are calculated based on temperature, density of gas and individual element abundances. We adopted the cooling rate from Wiersma et al. (2009) for optically thin gas in ionization equilibrium. Redshift-dependent UV/X-ray and cosmic microwave backgrounds with a modified Haardt & Madau (2012) spectrum are also included.

Stars are formed stochastically if the gas density exceeds a density threshold. This threshold is given as $n_{\rm th} \equiv n_0 \left(T_{\rm gas}/T_0\right)^3 \left(M_{\rm gas}/M_0\right)^2$ with $n_0 = 2.0{\rm cm}^{-3}$ and $T_0 = 12,000{\rm K}$, and M_0 is the gas particle mass. The star formation rate is calculated as ${\rm d}\rho_*/{\rm dt} = \eta\rho_{\rm gas}/{\rm t}_{\rm dyn}$, where ρ_*, $\rho_{\rm gas}$, and $t_{\rm dyn}$ are the stellar density, gas density, and local dynamical time for the gas particle, respectively. The star formation efficiency η and is set to 0.025.

Stellar feedback is included in the form of stellar winds and heating by ionizing radiation from young massive stars. Momentum from stellar winds is added to the surrounding gas particles, while cold gas within the Strömgren radius of hot stars is heated to $T = 10^4$ K.

In the supernova (SN) feedback model, a single SN event is assumed to eject mass in an outflow with a velocity $v_{\rm out,SN} = 4500\,{\rm km\,s^{-1}}$, a typical velocity of outflowing materials in SNe. SN energy and momentum are distributed to the surrounding interstellar medium (ISM) from the SN event. Depending on the distance to the SN events, each nearby gas particle is affected by one of three successive phases of SN remnant (SNR) evolution: the ejecta-dominated free expansion (FE) phase, the energy-conserving Sedov-Taylor blast-wave SNR phase, and the momentum-conserving snowplow phase. SN energy is transferred by conserving the ejecta momentum for gas particles within the radius of the FE phase. For gas particles lying outside the FE radius but within the Sedov-Taylor phase, the SN energy is transferred as 30% kinetic and 70% thermal. Finally, at larger radii in the snowplow phase, only a fraction of the original SN energy is transferred as radiative cooling becomes significant. See Appendix A of Núñez et al. (2017) for a detailed description of the implementation of the SN feedback model.

Feedback from low and intermediate initial mass stars via slow winds during an AGB phase is also included. Momentum and energy from old star particles are transferred to the neighboring gas particles in a momentum-conserving way. The outflowing wind velocity of AGB stars is assumed to be $v_{\rm out,AGB} = 10\,{\rm km\,s^{-1}}$, corresponding to typical outflowing velocities of AGB stars Nyman et al. (1992). Metal-enriched gas from all of these prescriptions is continuously added to the ISM. Metal diffusion, which allows for the mixing and spreading of metals in the enriched gas, is also included.

2.3 Black hole growth and feedback

In the simulations, the BHs are treated as collisionless sink particles and are seeded in newly forming dark matter halos. The dark matter halos are identified on the fly during a simulation by a friends-of-friends algorithm. The new BHs are seeded with mass of $10^5 h^{-1}{\rm M}_\odot$ such that any halo above $10^{11} h^{-1}{\rm M}_\odot$ contains one BH at its center if it does not already have a BH. The BH mass can then grow by gas accretion or by merging, when the two BHs fall within each other's local SPH smoothing lengths and their relative velocities are smaller than the local sound speed. Gas accretion onto the BH follows a Bondi-Hoyle-Littleton parametrization Bondi (1952).

The soft Bondi criterion introduced in Choi et al. (2012) is also included to avoid the unphysical accretion of unbound gas from outside the Bondi radius of the BH. This criterion statistically limits the accretion to the gas within the Bondi radius. It also accounts for the size of the gas particle as the physical properties of each gas particle are smoothed within the kernel size in the smoothed particle hydrodynamics simulations. Full accretion is only allowed when the total volume of a gas particle is included within the Bondi radius. If a gas particle volume is partially included within the Bondi radius, its probability of being absorbed by the BH is reduced. Finally, in order to account for the time that it takes to a particle to be accreted to a BH, the free-fall timescale is included following Choi et al. (2012).

Our AGN feedback model (Choi et al. 2012, 2014) consists of two main components:

(i) Mechanical feedback as in the broad absorption line winds, which carry energy, mass, and momentum into the surrounding gas. Winds are launched from the central region around the BH, with a fixed wind velocity of $v_{\rm outf,AGN} = 10,000\,{\rm km\,s^{-1}}$. The total energy flux carried by the wind is $\dot{E}_{\rm w} = \epsilon_{\rm w}\dot{M}_{\rm acc}c^2$, where the efficiency parameter $\epsilon_{\rm w}$ is set to 0.005 (Choi et al. 2017), $\dot{M}_{\rm acc}$ is the mass accretion rate onto the BH and c is the speed of light. The mass flux and momentum flux carried by the wind are $\dot{M}_{\rm outf} = 2\dot{M}_{\rm acc}\epsilon_{\rm w}c^2/v^2_{\rm outf,AGN}$. Thus, for our selected feedback efficiency $\epsilon_{\rm w}$ and wind velocity $v_{\rm outf,AGN}$, we have $\dot{M}_{\rm outf} = 9\dot{M}_{\rm acc}$. Therefore 90% of mass entering the central region is expelled, and 10% the inflowing mass is accreted onto the BH. The wind particles are stochastically selected among the particle entering the central region. The selected gas particles receive the wind kick in a direction parallel or antiparallel to their angular momentum vectors. The emitted wind particle shares its momentum with its two nearest neighbors to reproduce the shock-heated momentum-driven flows. The residual energy increases the temperature of the impacted gas particles; therefore, the total energy and momentum are conserved. This prescription gives a ratio of kinetic to thermal energy in the outflowing particles similar to that in the standard Sedov-Taylor blast wave.

(ii) Radiative feedback via the Compton and photoionization heating from the X-ray radiation from the accreting BH, the radiation pressure associated with the heating, and the Eddington force. The emergent AGN spectrum and metal-line heating are taken from Sazonov et al. (2004). X-ray radiation is coupled to the surrounding gas according to Sazonov et al. (2005). The radiation pressure on each gas element is also calculated. Accretion onto the BHs is not limited; the Eddington force is included, acting on electrons in the neighboring gas through the hydrodynamic equations, directed radially away from BH. In this way we allow that super-Eddington gas accretion occasionally occurs, so that the corresponding feedback effect naturally reduces the inflow and increases the outflow. Also included are metallicity-dependent heating prescriptions due to photoelectric emission and metal line absorption.

We refer the reader to Choi et al. (2017) for more details about our feedback prescriptions. See also Brennan et al. (2018) for an analysis of the wind properties and gas cycle in these simulations.

2.4 Zoom simulations

The initial conditions for the zoom-in simulations are described in Oser et al. (2010, 2012). The halos are picked from a dark matter only simulation using a flat cosmology with parameters obtained from from WMAP3 (Spergel et al. 2007; $h = 0.72$, $\Omega_{\rm b} = 0.044$, $\Omega_{\rm dm} = 0.216$, $\Omega_\Lambda = 0.74$,$\sigma_8 = 0.77$, $n_s = 0.95$). At any given snapshot we trace back all particles close to the halos of interest from redshift zero. We replace those particles with higher-resolution gas and dark matter particles. Then, new high-resolution initial conditions are simulated from redshift z = 43 to z = 0.

The simulations have been performed at two resolutions. The reference resolution has a mass resolution for the star and gas particles of $m_{*,\rm gas} = 4.2 \times 10^6\,{\rm h^{-1}M_\odot}$, and the dark matter particles have $m_{\rm dm} = 2.5 \times 10^7\,{\rm h^{-1}M_\odot}$. We

use the comoving gravitational softening lengths $\epsilon_{\rm gas,star}$ = 400 pc h^{-1} for the gas and star particles and $\epsilon_{\rm halo}$ = 890 pc h^{-1} for the dark matter. The high-resolution simulations have been performed with eight times better mass resolution than the reference resolution, with $m_{*,\rm gas} = 5.3 \times 10^5\,{\rm h}^{-1}{\rm M}_\odot$ and $m_{\rm dm} = 3.1 \times 10^6\,{\rm h}^{-1}{\rm M}_\odot$, and twice better spatial resolution with $\epsilon_{\rm gas,star} = 200\,{\rm pc\,h}^{-1}$ and $\epsilon_{\rm halo} = 450\,{\rm pc\,h}^{-1}$. In the Appendix, we discuss the resolution convergence.

The simulated halo masses are in the range $1.4 \times 10^{12}{\rm M}_\odot \leq {\rm M_{vir}} \leq 2.3 \times 10^{13}{\rm M}_\odot$ at z = 0, and the stellar masses of central galaxies are $8.2 \times 10^{10}{\rm M}_\odot \leq {\rm M}_* \leq 1.5 \times 10^{12}{\rm M}_\odot$ at present day.

In what follows, we will examine the satellite galaxies in zoom regions run with the two different models, wAGN and noAGN.

2.5 Halo and subhalo tracking

Dark matter halos were found using the ROCKSTAR algorithm from Behroozi et al. (2013). Halo masses were calculated using a spherical overdensity threshold fixed at 200 times that of the critical density at the considered redshift. The merger trees were computed using the ROCKSTAR CONSISTENT TREES.

3 RESULTS

Here we present the results of our analysis. First, in section 3.1 we examine the properties of the satellite galaxies at a various redshifts. Then, in section 3.2 we follow the main progenitors of the satellites found at redshift 0. Since we want to understand the effect of the central AGN, we exclude from our study the satellites in the wAGN simulations in which a BH has been placed, which could be quenched compared to their counterparts in the noAGN model independently from the central AGN. As a consequence, we also exclude from the noAGN sample the satellites that are above the mass threshold for BH seeding, in order to use the noAGN model as a control sample and to isolate the effect of the central AGN. We use a lower mass cut of 64 dark matter particles for selecting the satellites. We refer to the main halo of each zoom in simulation as the central galaxy even though we sometimes extend our study to neighboring galaxies that are outside the virial radius of the central galaxy. We use the `pygad` tool (Röttgers & Arth 2018) for our analysis.

3.1 Properties of the satellite galaxy population at various redshifts

3.1.1 Gas content and star formation

Fig. 1 shows the overall quiescent and gas poor fractions of the satellite galaxies as a function redshift: for each given redshift, we spotted in each zoom-in simulation the satellite galaxies within one virial radius of the main halo and computed the gas poor and quiescent fractions. We chose a specific star formation rate (SSFR) threshold of $10^{-11}{\rm yr}^{-1}$ for being quiescent, and a gas fraction threshold of 0.1 for being gas poor, the gas fraction being the ratio of the mass in gas to the mass in gas and stars ($M_{\rm gas}/(M_{\rm stars} + M{\rm gas}) < 0.1$), where

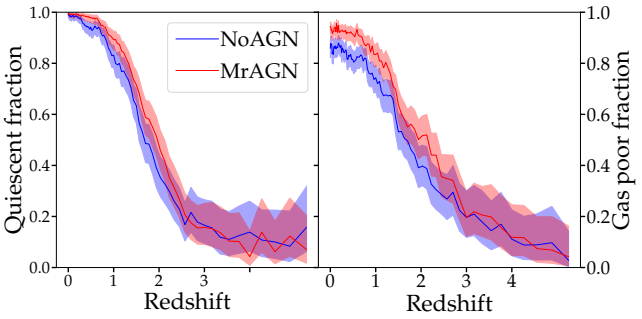

Figure 1. Comparison of the quiescent and gas poor satellite fractions in the wAGN and noAGN simulations. We stacked the satellites of the 28 zoom in simulations. Each redshift bin contains a few hundreds of satellites (~ 1000 at $z = 0$ and ~ 150 at $z = 3$). **Left**: Quiescent fraction (SSFR < $10^{-11}{\rm yr}^{-1}$) of the satellite galaxies within (within the virial radius of the central) as a function of redshift. **Right**: Gas poor fraction ($M_{\rm gas}/(M_{\rm stars} + M{\rm gas}) < 0.1$) of the satellite galaxies as a function of redshift. The error bars show the 99.7% confidence intervals computed for a beta distribution.

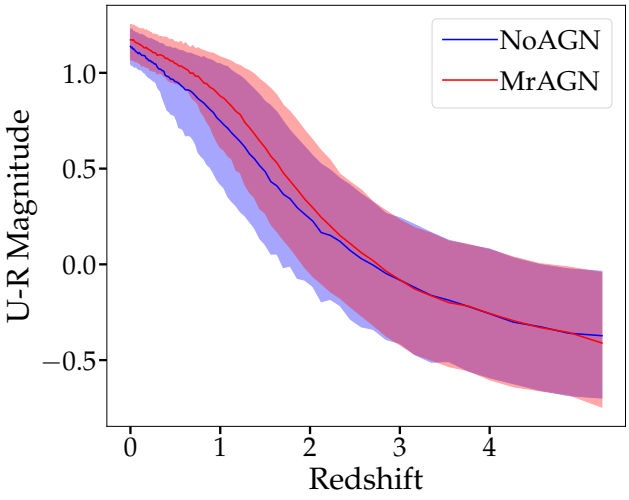

Figure 2. Comparison of the U - R magnitude of the satellite galaxies in the wAGN and noAGN simulations. We stacked the satellites of the 28 zoom in simulations. Each redshift bin contains a few hundreds of satellites (~ 1000 at $z = 0$ and~ 1000 at $z = 3$). The shaded area shows the 16% and the 84% percentiles of the distributions.

$M{\rm gas}$ and $M_{\rm stars}$ are measured within one tenth of the virial radius of the satellites. The error bars show the 99.7% confidence intervals computed as given by a beta distribution (Cameron 2011). Starting from $z = 2$ the difference between the wAGN and noAGN simulations grows. The quiescent fractions seem to be most significantly different from $z = 2$ to $z = 1$. At $z = 0$, the wAGN and noAGN satellites have quiescent fractions close to one. As for the gas poor fraction, the gas poor fractions are different from $z = 2$ and the difference between the noAGN and the wAGN keeps growing until $z = 0$.

Fig 2 shows the $U - R$ magnitude of the satellites computed using a `pygad` module that reads and interpolates

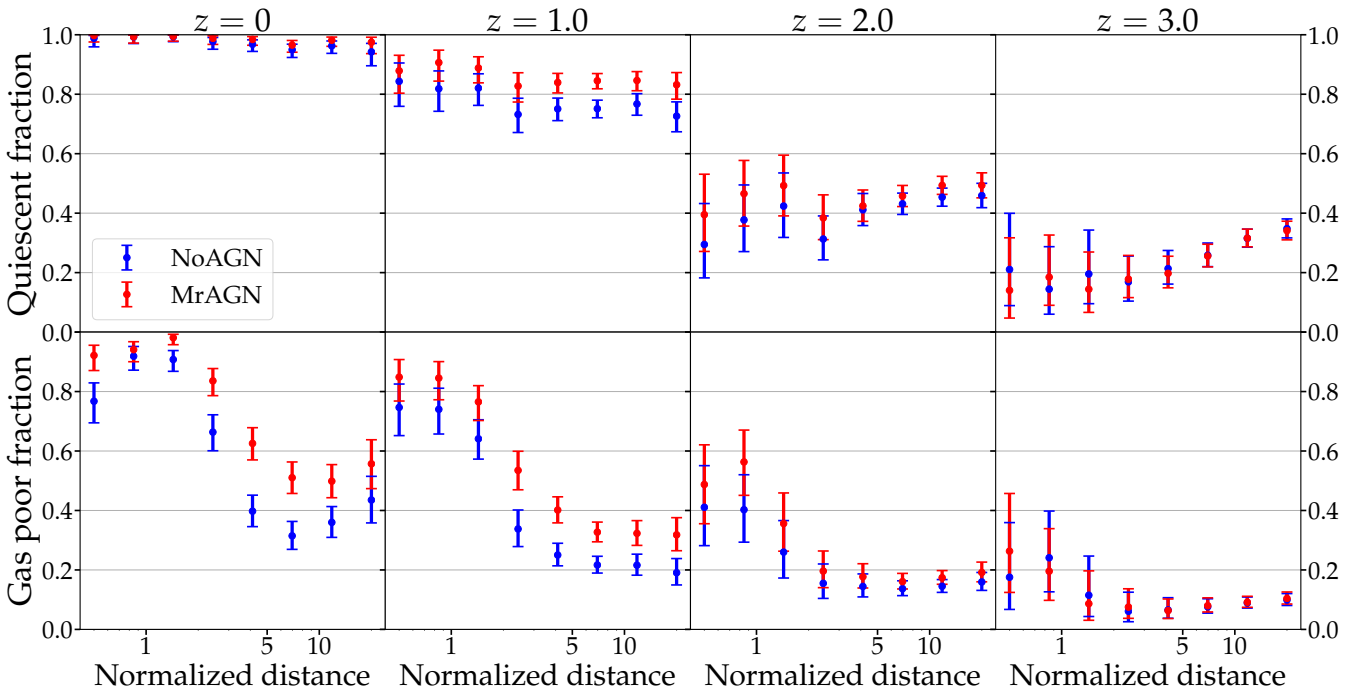

Figure 3. Quiescent and gas poor satellite fractions of the galaxies around the central as a function of the normalized distance to the central (distance to the central divided by the virial radius of the central). **Top** : Quiescent fractions (SSFR<10^{-11}yr^{-1}), the different panels show different redshifts. **Bottom**: Gas poor fractions ($M_{\rm gas}/(M_{\rm stars} + M{\rm gas}) < 0.1$). We stacked the satellites from the 28 zoom in simulations. The wAGN and noAGN samples each contain ∼ 4500 galaxies for z = 0,∼ 6000 galaxies for z = 1, ∼ 7000 galaxies for z = 2,∼ 7000 for z = 3. The error bars show the 99.7% confidence intervals computed for a beta distribution.

Bruzual & Charlot (2003) single stellar population model. The shaded area shows the 16% and the 84% percentiles of the distributions. The noAGN satellite population is bluer starting from z = 2, reflecting a more recent star formation, possibly impeded in the wAGN simulation by the presence of an AGN in the central galaxy.

3.1.2 Spatial extent of the quenching

Fig. 3 illustrates the quiescent and gas poor fractions of the galaxies around the central as a function of the normalized distance to the central (the distance to the central divided by the virial radius of the central). The upper panels show the evolution of the quiescent fraction in the wAGN et noAGN simulations, and the lower panels show the evolution of the gas poor fraction with thresholds for begin quiescent and gas poor identical to Fig. 1. The error bars show the 99.7% confidence intervals computed for a beta distribution. The quiescent and gas poor fractions are similar at z = 3 and the difference grows at lower redshifts, first out to 5 virial radius from the central galaxy at z = 2, then out to more than 10 times the normalized virial radius of the central galaxy at z = 1.

3.2 Histories of the main progenitors of the satellites

To gain more insight into the onset and time evolution of the quenching from the central AGN, we select, in each zoom halo, the neighboring galaxies that are within a sphere of twice the viral radius of the central at redshift 0 and trace back in time the main progenitor of these galaxies. Specifically, we follow their gas content and star formation history, as well as their distance to the central galaxy. As previously, we use a a lower mass cut of 64 dark matter particles for selecting the satellites, and we stop tracking back the satellites when their mass is below that threshold.

Fig 4 displays the stacked evolution of the gas mass of the main progenitor of the neighboring galaxies at z = 0 in different mass bins. In each bin of mass, the presence of an AGN in the central galaxy seems to alter the gas content of the neighboring galaxies. The maximum median and mean values of the distributions are lower for the wAGN simulations, perhaps suggesting a slightly reduced accretion onto the galaxies. Most importantly, the decrease of the gas content occurs earlier et more importantly in the wAGN simulation than in the noAGN simulation, indicating that the central AGN is involved in direct gas removal from the neighboring galaxies, or indirect removal through starvation.

Fig. 5 shows, as a function of cosmic time, the stacked evolution of the quiescent and gas poor fractions of the same traced back sample, in different mass bins. The difference in the stacked histories in the two wAGN and noAGN simulations develops at cosmic times of 4 to 8 Gyr, depending on the mass bin. The difference between noAGN and wAGN in gas poor and quiesent satellite fractions seems to pick at times of 6 to 10 Gyr depending on the mass bin.

Fig. 6 shows the same evolution as Fig. 5 a function of the distance to the central galaxy instead of cosmic time. We normalize that distance to the virial radius of the central

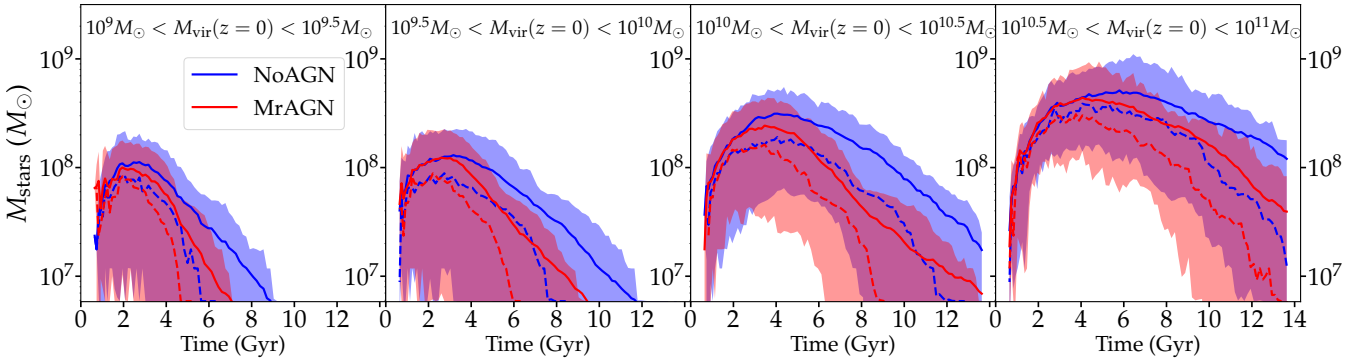

Figure 4. History of the gas mass of the galaxies that lie inside twice the virial radius of the central galaxy at $z = 0$ and traced back in time from $z = 0$, in different mass bins. Satellites are distributed in the different mass bins as a function of their virial mass at $z = 0$. We stacked the satellites from the 28 zoom in simulations. The different panels show increasing mass bins as indicated at the top of the upper panels and contain, from left to right: ~ 450, ~ 900,~ 270 and ~ 70 satellites. The shaded area shows the 16% and the 84% percentiles of the data. The solid lines are the mean values, and the dotted lines are the median values

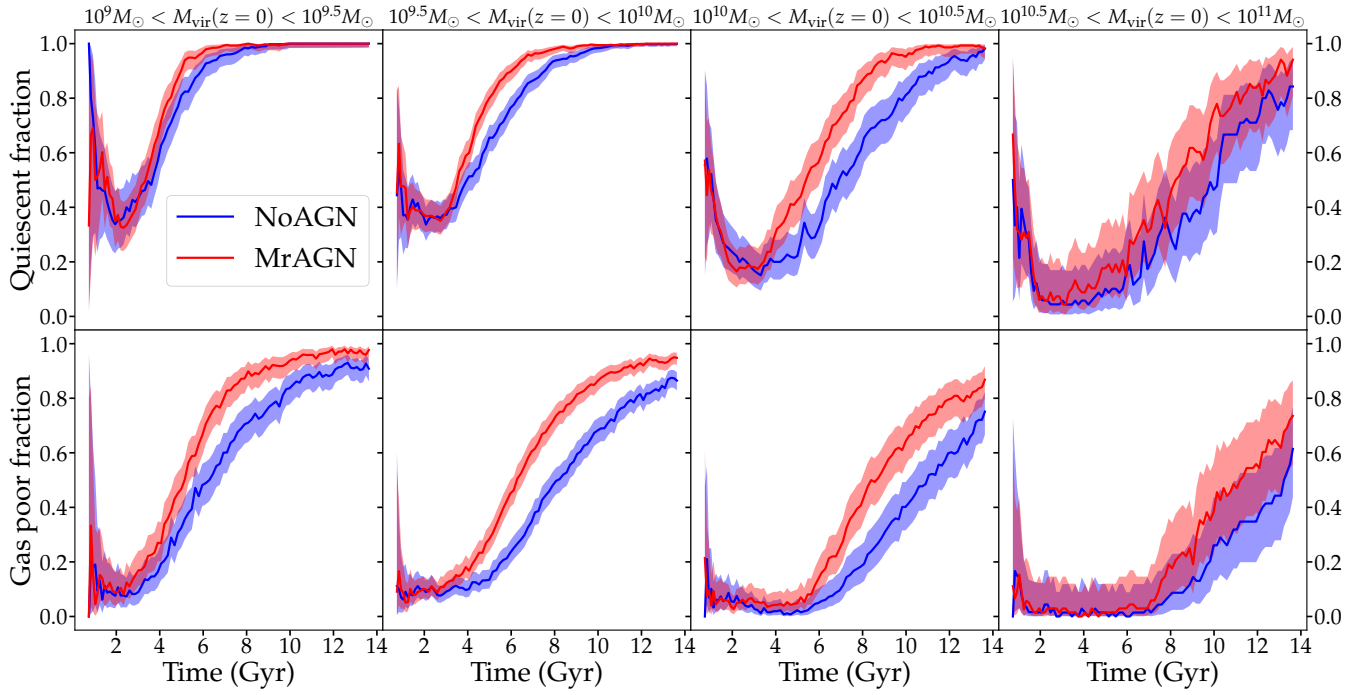

Figure 5. History of the quiescent and gas poor fractions of the galaxies that lie inside twice the virial radius of the central galaxy at $z = 0$ and traced back in time from $z = 0$, in different mass bins. Satellites are distributed in the different mass bins as a function of their virial mass at $z = 0$. We stacked the satellites from the 28 zoom in simulations. **Top** : Quiescent fraction (SSFR$<10^{-11}$yr^{-1}) as a function of time, from left to right the different panels show increasing mass bins as indicated at the top of the upper panels. **Bottom**: Gas poor fractions ($M_{gas}/(M_{stars} + M\,gas) < 0.1$) as a function of time. The different mass bins contain, from left to right: ~ 450, ~ 900,~ 270 and ~ 70 satellites. The error bars show the 99.7% confidence intervals computed for a beta distribution.

galaxy. Note that Fig. 6 is not a profile plot of the quiescent and gas poor fractions as a function of distance to the central at a given time: for each distance bin, the contribution of each galaxy to the distribution comes from different cosmic times. Note also that the distance plotted on the x axis is normalized to the virial radius of the central at th time where the distance is computed, which means that the physical value of that radius grows as a function of time, and that a given normalized distance is smaller in physical units at higher redshifts than lower redshifts because of the growth of the virial radius of the central galaxy. Fig. 6 shows that the normalized distance below which the wAGN and noAGN simulations differ is of 5 to 10 times the virial radius of the central galaxy. This means that the onset of the quenching by the central AGN occurs as early as when the galaxy is a distance from 5 to 10 times the virial radius of the central.

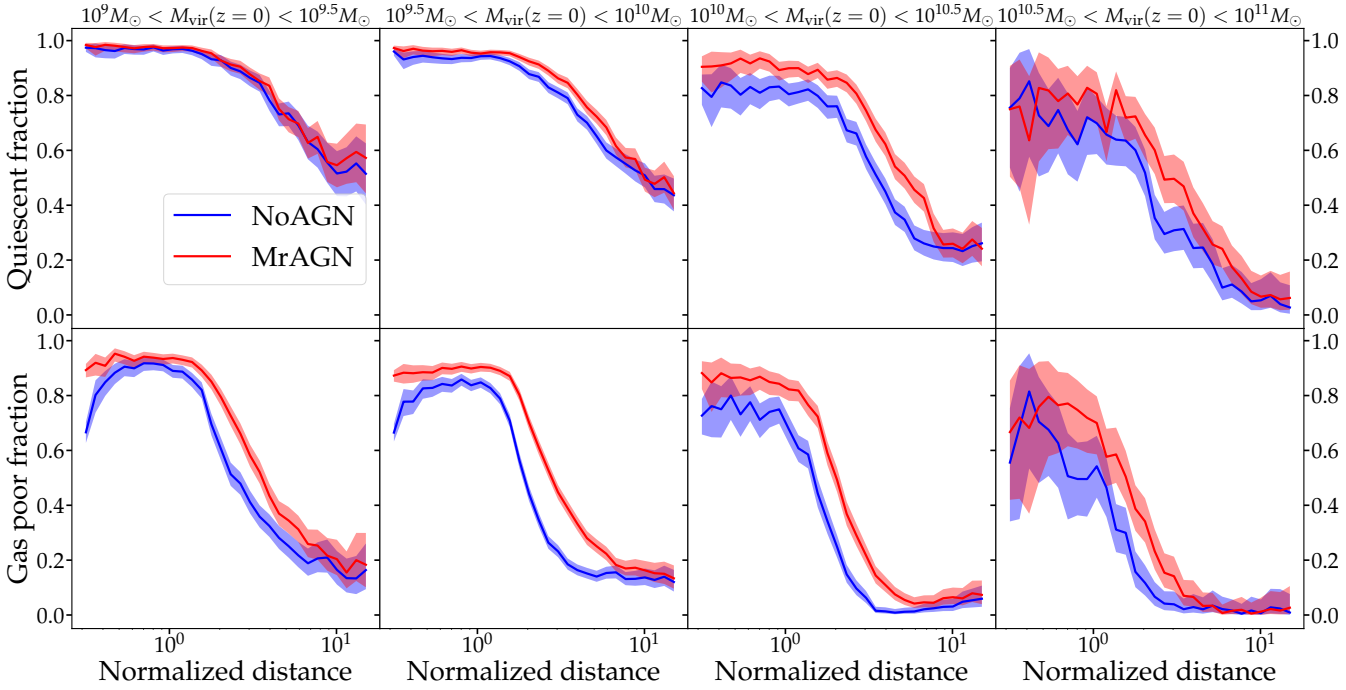

Figure 6. History of the quiescent and gas poor fractions of the galaxies that lie inside twice the virial radius of the central galaxy at $z = 0$ and traced back in time from $z = 0$, in different mass bins. Satellites are distributed in the different mass bins as a function of their virial mass at $z = 0$. We stacked the satellites from the 28 zoom in simulations. **Top** : Quiescent fraction (SSFR$<10^{-11}$yr^{-1}) as a function of time, from left to right the different panels show increasing mass bins as indicated at the top of the upper panels. **Bottom**: Gas poor fractions ($M_{\rm gas}/(M_{\rm stars} + M{\rm gas}) < 0.1$) as a function of time. The different mass bins contain, from left to right: ~ 450, ~ 900,~ 270 and ~ 70 satellites. The error bars show the 99.7% confidence intervals computed for a beta distribution.

4 DISCUSSION AND SUMMARY

In this work, we explore the possibility of an effect from the AGN of a central galaxy on its satellites. We used zoom-in simulations of 28 massive galaxies with halo masses of $10^{12-13.4} M_\odot$ at z = 0. We compared two sets on simulations: one that contains BHs and AGN feedback and one without BHs and without AGN feedback. Our noAGN model includes stellar feedback from multiple processes, including powerful winds from supernovae, stellar winds from young massive stars, and AGB stars, as well as radiative heating within Strömgren spheres, additional heating effects due to the presence of metals, including grain photoelectric heating and metallicity-dependent from the cosmic X-ray background. Our wAGN model is identical except that it also includes a model for BH seeding and accretion, as well as AGN feedback via high-velocity broad absorption line winds and Compton/photoionization heating. We use the noAGN simulations as a control sample to isolate the effect of the central AGN. We find that the inclusion of AGN feedback from centrals produces a significant difference in the evolution of the gas content and the star formation in the satellite galaxies, which suggests that AGN from the central might play a substantial role in the evolution of the satellite galaxy population. We also explore the spatial extent of this satellite quenching mechanism: we find that the difference between the two simulations extends as far out as a few times the viral radius of the central galaxy, suggesting that this effect could be relevant to models trying to reproduce the observed patterns of environmental quenching and perhaps to the physical origin of *galactic conformity*. We will explore the physics of this quenching mechanism in subsequent studies using idealized simulations.

ACKNOWLEDGEMENTS

This work was initiated as a project for the Kavli Summer Program in Astrophysics held at the Center for Computational Astrophysics of the Flatiron Institute in 2018. The program was co-funded by the Kavli Foundation and the Simons Foundation. We thank them for their generous support.

REFERENCES

Aumer M., White S. D. M., Naab T., Scannapieco C., 2013, MNRAS, 434, 3142
Bahé Y. M., McCarthy I. G., 2015, MNRAS, 447, 969
Behroozi P. S., Wechsler R. H., Wu H.-Y., 2013, ApJ, 762, 109
Bezanson R., van Dokkum P. G., Tal T., Marchesini D., Kriek M., Franx M., Coppi P., 2009, ApJ, 697, 1290
Bondi H., 1952, MNRAS, 112, 195
Brennan R., Choi E., Somerville R. S., Hirschmann M., Naab T., Ostriker J. P., 2018, ApJ, 860, 14
Bruzual G., Charlot S., 2003, MNRAS, 344, 1000
Buitrago F., Trujillo I., Conselice C. J., Bouwens R. J., Dickinson M., Yan H., 2008, ApJ, 687, L61
Calderon V. F., Berlind A. A., Sinha M., 2018, MNRAS,
Cameron E., 2011, Publ. Astron. Soc. Australia, 28, 128

Campbell D., van den Bosch F. C., Hearin A., Padmanabhan N., Berlind A., Mo H. J., Tinker J., Yang X., 2015, MNRAS, 452, 444
Choi E., Ostriker J. P., Naab T., Johansson P. H., 2012, ApJ, 754, 125
Choi E., Naab T., Ostriker J. P., Johansson P. H., Moster B. P., 2014, MNRAS, 442, 440
Choi E., Ostriker J. P., Naab T., Somerville R. S., Hirschmann M., Núñez A., Hu C.-Y., Oser L., 2017, ApJ, 844, 31
Choi E., Somerville R. S., Ostriker J. P., Naab T., Hirschmann M., 2018, preprint, (arXiv:1809.02143)
Cullen L., Dehnen W., 2010, MNRAS, 408, 669
Daddi E., et al., 2005, ApJ, 626, 680
Dekel A., Devor J., Hetzroni G., 2003, MNRAS, 341, 326
Durier F., Dalla Vecchia C., 2012, MNRAS, 419, 465
Farouki R., Shapiro S. L., 1981, ApJ, 243, 32
Gunn J. E., Gott III J. R., 1972, ApJ, 176, 1
Haardt F., Madau P., 2012, ApJ, 746, 125
Hearin A. P., Watson D. F., van den Bosch F. C., 2015, MNRAS, 452, 1958
Hearin A. P., Behroozi P. S., van den Bosch F. C., 2016, MNRAS, 461, 2135
Hirschmann M., Naab T., Somerville R. S., Burkert A., Oser L., 2012, MNRAS, 419, 3200
Hopkins P. F., 2013, MNRAS, 428, 2840
Hu C.-Y., Naab T., Walch S., Moster B. P., Oser L., 2014, MNRAS, 443, 1173
Kauffmann G., 2015, MNRAS, 454, 1840
Kauffmann G., 2018, MNRAS, 475, L45
Kauffmann G., Li C., Heckman T. M., 2010, MNRAS, 409, 491
Kauffmann G., Li C., Zhang W., Weinmann S., 2013, MNRAS, 430, 1447
Kimm T., et al., 2009, MNRAS, 394, 1131
Knobel C., Lilly S. J., Woo J., Kovač K., 2015, ApJ, 800, 24
Larson R. B., Tinsley B. M., Caldwell C. N., 1980, ApJ, 237, 692
Moore B., Lake G., Katz N., 1998, ApJ, 495, 139
Naab T., Johansson P. H., Ostriker J. P., Efstathiou G., 2007, ApJ, 658, 710
Núñez A., Ostriker J. P., Naab T., Oser L., Hu C.-Y., Choi E., 2017, ApJ, 836, 204
Nyman L.-A., et al., 1992, A&AS, 93, 121
Oser L., Ostriker J. P., Naab T., Johansson P. H., Burkert A., 2010, ApJ, 725, 2312
Oser L., Naab T., Ostriker J. P., Johansson P. H., 2012, ApJ, 744, 63
Peng Y.-j., et al., 2010, ApJ, 721, 193
Peng Y.-j., Lilly S. J., Renzini A., Carollo M., 2012, ApJ, 757, 4
Phillips J. I., Wheeler C., Boylan-Kolchin M., Bullock J. S., Cooper M. C., Tollerud E. J., 2014, MNRAS, 437, 1930
Read J. I., Hayfield T., 2012, MNRAS, 422, 3037
Röttgers B., Arth A., 2018, preprint, (arXiv:1803.03652)
Saitoh T. R., Makino J., 2009, ApJ, 697, L99
Sales L. V., Navarro J. F., Theuns T., Schaye J., White S. D. M., Frenk C. S., Crain R. A., Dalla Vecchia C., 2012, MNRAS, 423, 1544
Sazonov S. Y., Ostriker J. P., Sunyaev R. A., 2004, MNRAS, 347, 144
Sazonov S. Y., Ostriker J. P., Ciotti L., Sunyaev R. A., 2005, MNRAS, 358, 168
Sin L. P. T., Lilly S. J., Henriques B. M. B., 2017, MNRAS, 471, 1192
Somerville R. S., Davé R., 2015, ARA&A, 53, 51
Spergel D. N., et al., 2007, ApJS, 170, 377
Springel V., 2005, MNRAS, 364, 1105
Szomoru D., Franx M., van Dokkum P. G., 2012, ApJ, 749, 121
Tinker J. L., Hahn C., Mao Y.-Y., Wetzel A. R., Conroy C., 2018, MNRAS, 477, 935
Tonnesen S., Bryan G. L., 2009, ApJ, 694, 789

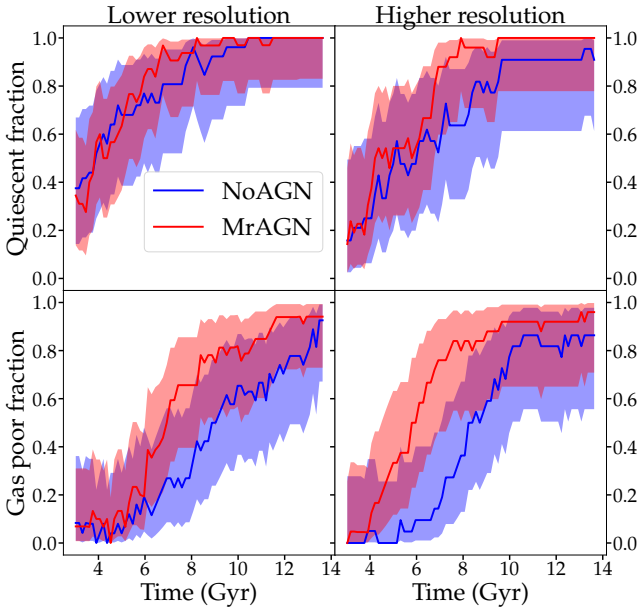

Figure A1. Test of the convergence with respect to resolution using two realizations of two halos that have been run with eight times better mass resolution than the reference resolution, with $m_{*,\rm gas} = 5.3 \times 10^5\,{\rm h^{-1}M_\odot}$ and $m_{\rm dm} = 3.1 \times 10^6\,{\rm h^{-1}M_\odot}$, and twice better spatial resolution with $\epsilon_{\rm gas,star} = 200\,{\rm pc\,h^{-1}}$ and $\epsilon_{\rm halo} = 450\,{\rm pc\,h^{-1}}$. The upper panels show the quiescent fractions of satellites galaxies as a function of time, for the lower (left) and the higher resolution simulation (right). The lower panels show the gas poor fractions for the lower (left) and the higher resolution simulation (right)

Trujillo I., et al., 2006, ApJ, 650, 18
Wang W., White S. D. M., 2012, MNRAS, 424, 2574
Wechsler R. H., Tinker J. L., 2018, preprint, (arXiv:1804.03097)
Weinmann S. M., van den Bosch F. C., Yang X., Mo H. J., 2006, MNRAS, 366, 2
Wetzel A. R., White M., 2010, MNRAS, 403, 1072
Wiersma R. P. C., Schaye J., Smith B. D., 2009, MNRAS, 393, 99
van Dokkum P. G., et al., 2010, ApJ, 709, 1018

APPENDIX A: RESOLUTION STUDY

We test the with respect to resolution using two realizations of two halos that have been run with eight times better mass resolution than the reference resolution, with $m_{*,\rm gas} = 5.3 \times 10^5\,{\rm h^{-1}M_\odot}$ and $m_{\rm dm} = 3.1 \times 10^6\,{\rm h^{-1}M_\odot}$, and twice better spatial resolution with $\epsilon_{\rm gas,star} = 200\,{\rm pc\,h^{-1}}$ and $\epsilon_{\rm halo} = 450\,{\rm pc\,h^{-1}}$. One sees that the difference in quiescent and gas poor fractions holds for the higher resolution simulation.

This paper has been typeset from a TEX/LATEX file prepared by the author.